Advances in Water Resources 214 (2026) 105367

Contents lists available at ScienceDirect

Advances in Water Resources

journal homepage: www.elsevier.com/locate/advwatres

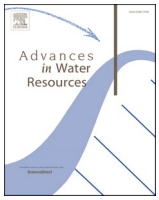

Evaporation-induced Marangoni effect reshapes flow-by drying of porous matrix adjacent to a gas-flowing fracture

Yandong Zhang [a,e,1,*], Fei Yu [b,c,e,1], Shuai Zheng [d,e], Bowen Ling [a], Dongxiao Zhang [e,f], Ke Xu [e,**]

[a] Institute of Mechanics, Chinese Academy of Science, Beijing 100190, China
[b] Sinopec Key Laboratory of Drilling Completion and Fracturing of Shale Oil and Gas, Beijing 102206, China
[c] Sinopec Research Institute of Petroleum Engineering Co., Ltd., Beijing 102206, China
[d] Research Institute of Petroleum Exploration and Development, Beijing 100089, China
[e] Department of Energy and Resources Engineering, School of Mechanics and Engineering Science, Peking University, Beijing 100871, China
[f] Ningbo Institute of Digital Twin, Eastern Institute of Technology, Ningbo, Zhejiang, 315200, China

ARTICLE INFO

Keywords:
Flow-by drying
Porous media
Evaporation-induced Marangoni effect
Gas–liquid displacement
Subsurface multiphase flow

ABSTRACT

During CO_2 sequestration, hydrogen storage and geothermal recovery, dry gas flows through subsurface porous media saturated with volatile liquid along high-permeability pathway, and vaporizes liquid in neighboring porous matrix. We conduct microfluidic experiments to investigate the drying kinetics of this fracture-adjacent process, here denoted flow-by drying, in which the air flows primarily through a neighboring fracture while drying the porous matrix by evaporation. We surprisingly discover a counter-intuitive "inside-out" drying pattern, that air invades deep inside the porous matrix and maintains a liquid-saturated belt along the air preferential path. Its emergence is attributed to Marangoni effect, as a consequence of evaporation-induced temperature gradient. This "inside-out" drying reshapes drying kinetics by decoupling evaporation front from displacement front and keeping effective evaporation area unchanged. In addition, we also identify a quasi-isothermal evaporation regime and a viscous displacement regime. Boundaries between the three regimes are theoretically estimated, which well matches experimental results. This new discovery highlights the necessity to take thermal effect into consideration during modeling subsurface hydrological processes with extensive phase changes.

1. Introduction

Displacement of volatile liquid by gas in porous media is a typical scenario in various subsurface applications such as CO_2 sequestration in deep saline aquifers (Peysson et al., 2014), hydrogen and natural gas subsurface storage (Zivar et al., 2021; Krevor et al., 2023), and recovery of geothermal energy or hydrocarbons from underground reservoirs (Sim et al., 2009; Kamath and Laroche, 2003; Mahadevan and Sharma, 2003). Gas can induce evaporation of liquid in porous media, that results so called "flow-through drying" (Allerton, 1948; Jagannathan et al., 2006). During flow-through drying, spatial distribution and composition of the liquid accordingly evolves, that may induce complicated subsequential physical, chemical and biological changes (Ott et al., 2014; Ott et al., 2015).

Evaporation in porous media without gas flow-through has been extensively investigated (Attari Moghaddam et al., 2017; Chauvet et al., 2009; Pillai et al., 2009; Prat, 2011; Ahmad et al., 2021; Chraibi et al., 2009; Prat, 2007; Vorhauer et al., 2015). Such isothermal and quasi-static evaporation is mostly diffusion-driven, that can be divided into sequential three stages (Chauvet et al., 2009). Initially, a constant rate period (CRP) emerges that the evaporating interface is directly contacting the open space, which can be maintained by wetting films (Lehmann et al., 2008; Yiotis, 2005; Scherer, 1990; Shokri et al., 2009). When the region close to open surface dries out, the evaporation turns into the falling rate period (FRP) when the internal mass transfer becomes significant. When the gas-liquid interface is so far away from the

* Corresponding author at: Institute of Mechanics, Chinese Academy of Science, Beijing 100190, China.
** Corresponding author.
E-mail addresses: zhangyd@imech.ac.cn (Y. Zhang), kexu1989@pku.edu.cn (K. Xu).
[1] Yandong Zhang and Fei Yu contribute equally to this work.

https://doi.org/10.1016/j.advwatres.2026.105367
Received 12 February 2026; Received in revised form 25 May 2026; Accepted 27 May 2026
Available online 28 May 2026

open space that internal mass transfer limits the drying, the drying falls into receding front period (RFP) that the drying rate slows down with the square root of time. With more complex boundary conditions, there can be more factors involving (Lehmann et al., 2008; Prat, 2002). Classical one-side-open micromodel evaporation studies have further shown that drying typically proceeds through the development of a dry region near the open boundary, a partially wet film region, and a fully saturated region deeper in the porous medium, with the drying front receding progressively away from the open side. Representative benchmark studies have emphasized the roles of corner flow, thick-film flow, surface roughness, and wettability in controlling this conventional front-recession picture (Ding and Geistlinger, 2021; Geistlinger et al., 2019).

In flow-through drying, however, the kinetics is highly complicated by stronger viscous effects and more extensive phase change. It has been found that gas flowing across the conduit/fracture-porous media interface could cause higher evaporation efficiency than expectation, that more liquid is evaporated before the fracture-matrix interface becomes dry (Mahadevan et al., 2006), while the underlying mechanisms have not been not fully resolved. One noticeable fact is that evaporation is endothermic, so the evaporation front can be cooled down which generates local temperature gradient (Huinink et al., 2002). Unfortunately, in field-scale simulation, high local gradient cannot be captured directly due to the limitation of grid size (Vilarrasa and Rutqvist, 2017; Andersen and Nilsen, 2018; Milly, 1984). Microscopic scale investigation is thus required. It has been highlighted that temperature gradient induces Marangoni effect that modify fluid-fluid displacement pattern at pore-scale (D'Aubeterre et al., 2005; Huinink et al., 2002; Gourbil et al., 2019; Plourde and Prat, 2003; Surasani et al., 2008; Surasani et al., 2008; Surasani et al., 2009; Surasani et al., 2010; Vorhauer et al., 2018), due to negative correlation between capillary pressure and temperature. However, temperature gradient in proceeding microscopic studies is imposed by adding external heat sources, which is very different from that in flow-through drying, where the temperature gradient is directly connecting to the evaporation kinetics as well as the spatial morphology of evaporation front. The role of evaporation-induced temperature gradient in flow-through drying is still largely unexplored.

In this study, the gas-induced drying process also occurs through a fracture–matrix configuration. Specifically, the gas flows primarily through the upper fracture and induces evaporation and desaturation in the adjacent porous matrix, rather than flowing uniformly through the entire porous network. To distinguish this configuration from conventional flow-through drying, in which the gas flows directly through the porous network, we refer to the present process as flow-by drying. This term is used throughout this paper to emphasize the fracture-adjacent nature of the drying process. Our goal is to clarify how evaporation-induced thermal effect reshapes the corresponding drying kinetics in porous media, pore-scale invasion morphology, fluid distribution evolution and relevant physical and chemical processes. To isolate and visualize these thermal effects more clearly, we employ a highly volatile liquid that amplifies evaporation-induced cooling under laboratory conditions. The paper is organized as follows: 1) we describe the details of the experimental design, set-up and data analysis methods; 2) we show the experimental observation about evaporation patterns at different gas flow rates and discuss their implications, especially in regimes that evaporation-induced thermal effect takes dominance; 3) we theoretically identify the boundaries between different drying regimes and validate the theory with experiment; and 4) we discuss the geophysical significance to bring in consideration of evaporation-induced thermal effect.

2. Setup and methods

2.1. Experimental setup

We design a glass microfluidic model consisting of a highly conductive fracture, and a homogeneous porous matrix which is exposed to the fracture at one side, as demonstrated in Fig. 1a. The other three boundaries of the porous matrix are closed for simplicity. The fracture width is $w_f = 0.5$ mm. The porous matrix length parallel to the fracture is $l = 6$ mm and the porous matrix width is 3 mm, that consists of an array of cylindrical posts with diameter $d_p = 0.1$ mm and the pore-throat width is $w_t = 0.05$ mm. The depth for all flow paths is $h = 0.02$ mm. The porosity of the porous media is 55%. The fabrication-induced throat size contrast was quantified from optical microscope measurements after calibration with a standard stage micrometer. After converting the image scale from pixels to micrometers, the widths of multiple representative throats across the micromodel were measured and compared with the nominal design value. The nominal throat width is $w_t = 0.05$ mm, and the measured fabrication deviation is approximately $\Delta w_t = 1$ μm, corresponding to about 2% of the nominal throat width. The thickness of the glass microfluidic chip is $z_g = 4$ mm (2 mm for each side of the channel), and the glass thermal conductivity is $\kappa = 0.9$ W/K/m. This design is to analog 1) fractured subsurface porous media, and 2) gas diffusion layer in fuel cell (Carmo et al., 2013; Park et al., 2015; Jiao et al., 2021).

We note that the three closed boundaries of the porous matrix are slightly wider than the internal pore throats, most likely due to local over-etching or fabrication-induced widening near the chip boundary. These widened peripheral regions may have lower capillary entry pressure than the regular internal pore network and can therefore promote earlier local air entry along the side and bottom boundaries. This geometric feature imposes asymmetric boundary conditions for fluid retained in the rest of the porous region, that can help to explore the mechanisms at different flow conditions as discussed in following Results section.

We conduct all our glass-micromodel experiments under nominal ambient laboratory conditions. The laboratory air conditioner is set to 20 °C, and the room relative humidity is monitored using a laboratory hygrometer, with a typical value of approximately 35% during the experiments. Atmospheric pressure ($P = 1$ atm) is used as the air pressure boundary condition. These ambient conditions are not varied as experimental parameters in this study. The defending fluid we choose is pentane (chromatographic-grade, Sigma-Aldrich, ≥99.9%) for its highly evaporable property, which amplifies evaporation-induced cooling and interfacial thermal effects, allowing the corresponding mechanism to be directly visualized within laboratory time scales. We use air as the carrier gas to provide a simple and well-controlled gas-phase environment for the microfluidic experiments. The vapor pressure of pentane at this condition is $p_v \approx 56.55$ kPa, the latent heat for evaporation is $\lambda = 3.9 \times 10^5$ J/kg, and the molar mass is $M_g = 0.072$ kg/mol. To clear the dissolved gas bubbles in pentane, we saturate the pentane on a hotplate with several rounds of injection and evaporation to fill the whole porous media with pentane vapor. We pose the micromodel flatwise so gravitational effect can be neglected (Surasani et al., 2009), as the Bond number $Bo = \frac{\Delta\rho g h^2}{\sigma} \ll 1$, where $\Delta\rho$ is the density difference between air (1.29 kg/m^3) and pentane (626kg/m^3), $g = 9.8$ m/s^2 is the gravity constant and σ is the surface tension. Under the experimental condition, surface tension between air and pentane is $\sigma = 15.5$ mN/m, and its temperature dependence is $\frac{\partial\sigma}{\partial T} = -0.11$ mN/m/K (Grigoryev et al., 1992).

We use syringe pump (Harvard PHD ULTRA 80-4415 CP) to precisely control the air flow rates. The air first displaces the defending fluid in the conductive fracture in a very short time, and then gradually evaporates and displaces the liquid in the porous matrix. We start the video recording right after the fracture is saturated with 100% of air. A typical

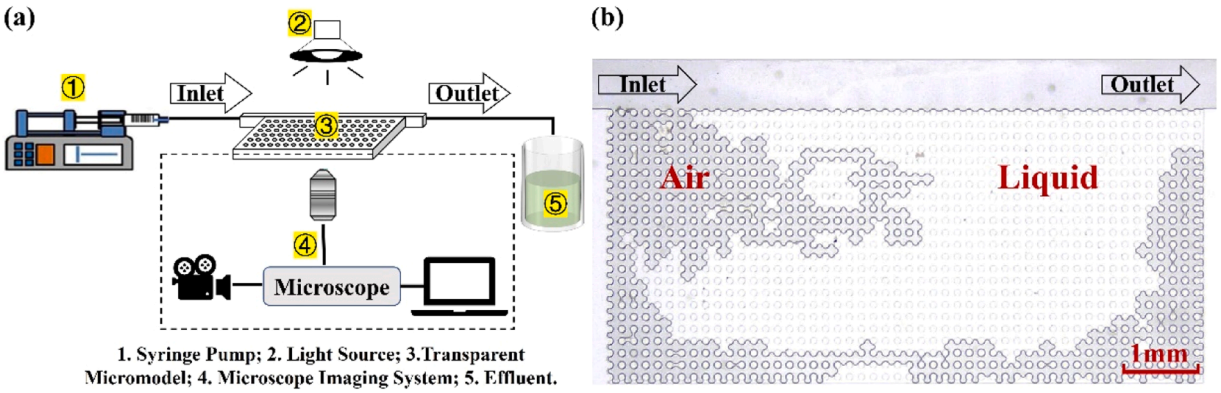

Fig. 1. (a) Schematic illustration of the microfluidic experiment setup. (b) A typical image on the microfluidic model captured during the flow-by drying experiment. Dark regions indicate air-filled pores, whereas light/transparent regions indicate liquid-filled regions.

image during the microfluidic experiment is shown in Fig. 1b when air saturation is about 60% in porous matrix. According to the color difference between the air and liquid, we are able to quantify the evolution of air saturation in porous media over time.

2.2. Key variables

We conduct demonstrated experiments under three cases, where we adjust air injection rate (q_{air}) as 3×10^{-6} ml/min (case 1), 8×10^{-4} ml/min (case 2)and 0.6 ml/min (case 3), respectively. The corresponding capillary numbers ($Ca = \frac{\mu v_{air}}{\sigma}$ where $\mu = 3 \times 10^{-4}$ Pa·s is the air viscosity and $v_{air} = \frac{q_{air}}{hw_f}$ is the air velocity if it flows only along fracture) of these three cases are 9.7×10^{-8}, 2.6×10^{-5},1.9×10^{-2}, respectively (Hilfer and Øren, 1996).

In addition, to compare the viscous dissipation along the fracture, $\Delta p_{vis} \sim \frac{\mu v_{air} l}{h^2/12}$, and the capillary entrance pressure into porous matrix, $p_c = \frac{2}{w_t}\sigma$, we define a modified capillary number $Ca_f = \frac{\Delta p_{vis}}{p_c} = \frac{6lw_t}{h^2}Ca$, where f denotes the fracture. Values of Ca_f in three cases are 4.4×10^{-4}, 0.12 and 87.3, respectively. If Ca_f<1, all displacement in porous matrix can be attributed to evaporation; otherwise, viscous force can also mobilize the liquid in porous matrix.

2.3. Tracking the trajectory of liquid mass center

To better characterize the evaporation pattern, we plot the trajectories of liquid mass centers versus evaporation time. At the beginning,

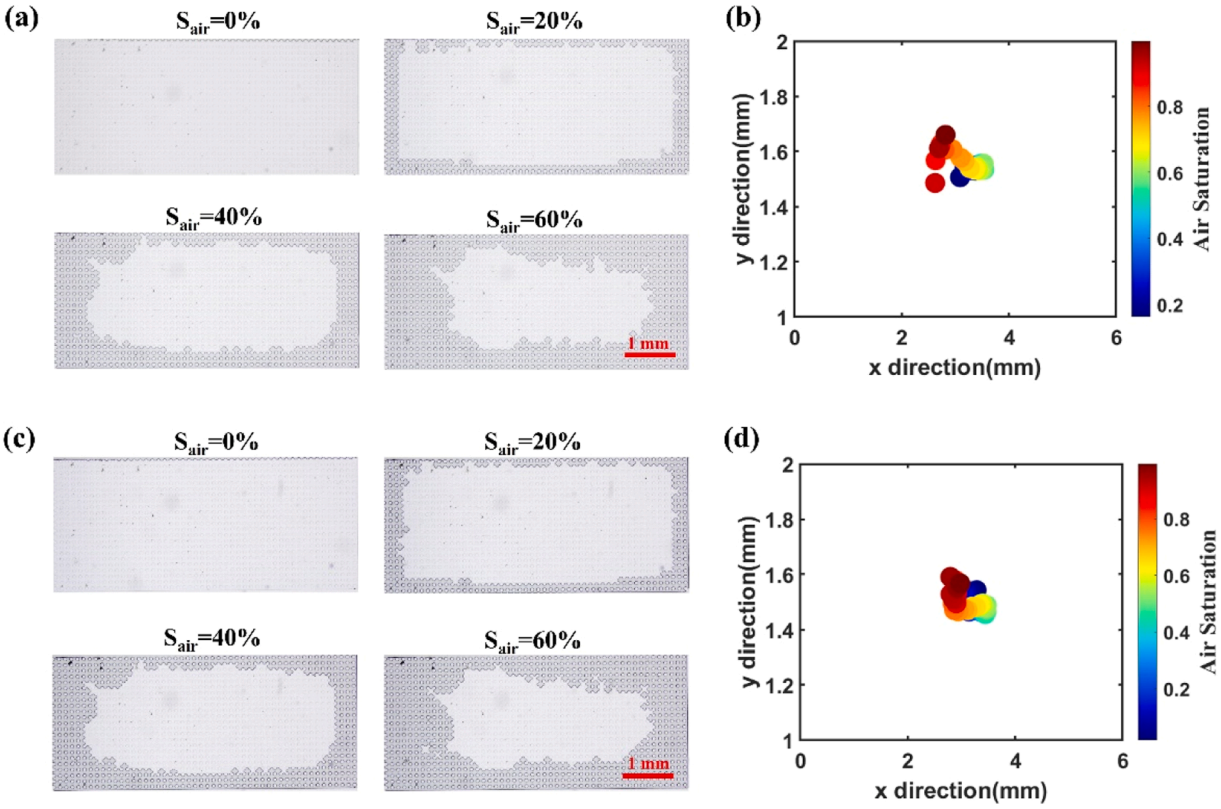

Fig. 2. (a) Original experimental image of case 1 at different moments; (b) mass center trajectory during case 1; (c) original experimental image of the parallel experiment of case 1 using isoheptane at different moments; (d) mass center trajectory during the parallel experiment of case 1 using isoheptane. Dark regions indicate air-filled pores, whereas light/transparent regions indicate liquid-filled regions.

the mass center point stays in the middle of the model when the model is fully saturated with liquid. We track the mass center point as the increase of the air saturation and with different colors at different air saturations. All the original experimental videos are provided in supplementary files.

3. Experimental results

As abovementioned, we conduct three sets of experiments to perform different evaporation patterns under different air flowrates. For case 1&2, we also conduct parallel experiments using isoheptane, which is of much lower vapor pressure (≈6.89 kPa), for comparison.

3.1. Case 1: quasi-isothermal evaporation

In case 1 ($q_{air} = 3 \times 10^{-6}$ mL/min, $Ca = 9.7 \times 10^{-8}$, $Ca_f = 4.37 \times 10^{-4}$), the air invades into the porous media in a relatively compact recession pattern with a rough interface, and forms a dry fracture/matrix interface soon after the onset of the evaporation process, as shown in Fig. 2a. The distance between the evaporation front and the fracture keeps increasing. Drying in case 1 shows no strong lateral bias, as shown in the evolution of pentane mass center trajectory (Fig. 2b) that the liquid mass center moves very slightly near the center.

It should be noted that drying pattern is very symmetric, although the gas flow rate in the fracture is much higher than through the side and bottom boundaries. Such asymmetric boundary does not induce asymmetric drying, indicating that neither momentum transfer nor mass transfer affect fluid perturbation sequence under such low flow rate. This also matches with the observation that similar drying pattern is reproduced in the parallel experiment using isoheptane that is more difficult to evaporate with much longer drying time, as shown in Fig. 2c, d.

We thus conclude that evaporation and corresponding thermal effect can be neglected in this case. We consequently denote case 1 by "isothermal evaporation" and use case 1 as a reference.

3.2. Case 2: "inside-out" drying

In case 2 ($q_{air} = 8 \times 10^{-4}$ mL/min $Ca = 2.58 \times 10^{-5}$, $Ca_f = 0.12$), we observe very different evaporation pattern from that in case 1 (isothermal evaporation). As shown in Fig. 3a, the displacement front keeps penetrating inside the porous matrix after air invading, without desaturating the liquid near the matrix-fracture interface. Note that the irregular penetrating path in our homogeneous porous media is caused by local capillary instabilities (Edery et al., 2018). Only after drying out of the deeper liquid, when air saturation is >60%, mild drying at the matrix-fracture interface starts. During this "inside-out" evaporation, the mass center keeps moving towards the fracture, as shown in Fig. 3b

By "inside-out", we do not mean that evaporation literally initiates from the three closed sides. Here, "inside" and "out" are defined relative to the fracture-matrix configuration: 'inside' refers to the porous matrix interior, whereas 'out' refers to the fracture-side boundary of the matrix. Therefore, the term "inside-out" does not mean drying from the three closed outer boundaries, but rather that matrix-interior gas invasion becomes pronounced before complete local dry-out occurs at the fracture-side boundary.

The widened peripheral boundaries still promote recession from the side and bottom closed boundaries in this case at very early stage. However, unlike the symmetric fluid recession pattern in the low-flow case 1, the drying pattern becomes asymmetric in y-direction: gas starts to invade from the fracture side into the matrix interior, while the liquid near the fracture-porous media interface remains connected and

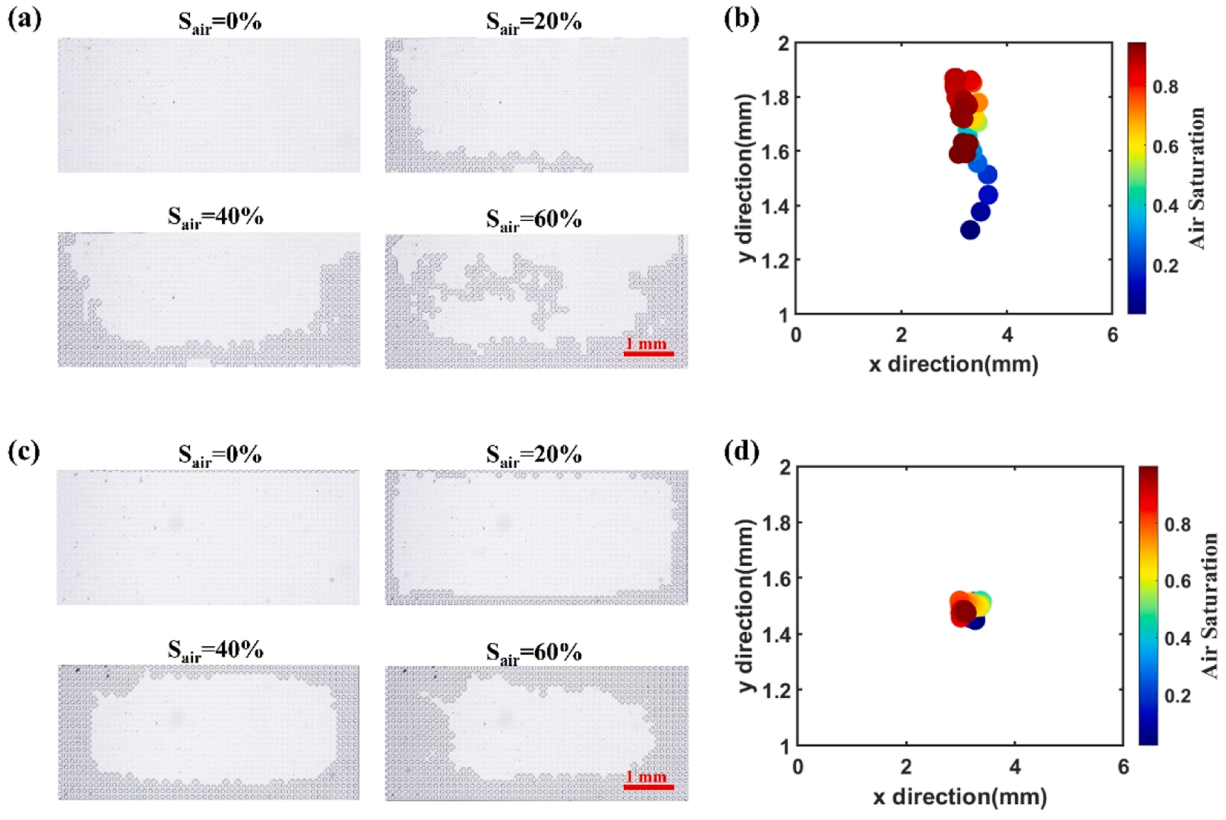

Fig. 3. (a) Original experimental image of case 2 at different moments; (b) mass center trajectory during case 2; (c) original experimental image of the parallel experiment of case 2 using isoheptane at different moments; (d) mass center trajectory during the parallel experiment of case 2 using isoheptane; Dark regions indicate air-filled pores, whereas light/transparent regions indicate liquid-filled regions. Only the pentane case in panel (a) is classified as inside-out drying; the isoheptane control in panel (c) still shows a geometry-modified receding-front pattern.

wet for a much longer time. Simultaneously, the pattern is still highly symmetric in x-direction. It strongly indicates the dominant role of mass transfer/phase change and negligible effect of viscous effect (momentum transfer) in shaping the fluid recession pattern.

This conclusion is further confirmed by the observation of the isoheptane control experiment under the same flow rate in Fig. 3c, d, where the drying front still recedes compactly from the fracture side and three closed boundaries because of the widened peripheral channels.

3.3. Case 3: convective drying

We further increase the air flow rate in case 3 ($q_{air} = 6 \times 10^{-1}$ mL/min, $Ca = 1.94 \times 10^{-2}$, $Ca_f = 87.3$), that $Ca_f >> 1$. The displacement becomes mainly left to right, while the "inside-out drying" morphology is only observed in very late time, when liquid loses continuity and becomes discrete clusters, as shown in Fig. 4a. Under this high-flow condition, the mass center trajectory shows stronger fluctuations, suggesting that the invasion process becomes more unstable with viscous effects dominated. Although non-classical morphology persists in Cases 3, the dominant control is no longer identical to that of Case 2 because viscous air-flow effects become increasingly important.

In the high-flow case, the peripheral recession becomes much less apparent because the strong imposed air flow rapidly disrupts this pathway and drives air invasion into the matrix interior. The system becomes highly asymmetric in x-direction, indicating that viscous effect is dominant.

3.4. Summary of experimental observations

In above experiments, we vary Ca by more than six orders of magnitudes, that covers major range of concern in most geophysical applications relevant to flow-through drying. Our major discovery is the emergence of "inside-out" drying pattern, which appears when evaporation rate is adequately extensive. When Ca is extremely large, however, viscous displacement effects dominate and the "inside-out" pattern can only be observed in late time when liquid loses continuity and becomes discrete clusters.

To further visualize the temporal evolution of the invasion pattern, cumulative air-invasion maps are provided in the Supplementary Information (Fig. S5), where the color indicates the first time at which each pore (or local region) becomes air-invaded. These maps complement the representative snapshots in the main text and help distinguish the classical front recession observed in the low-flow cases from the non-classical inside-out morphology observed in the higher-flow pentane cases.

4. Theory and discussion

4.1. Hypothesis

The evaporation of volatile liquid cools down the fracture-matrix interface, results in a temperature contrast between the fracture and deep porous matrix (See Figure S2 for our temperature measurement using infrared camera). The temperature contrast leads to surface tension contrast, $\Delta\sigma_T$. As $\partial\sigma/\partial T < 0$, the capillary entrance pressure ($p_c = \frac{2}{w_t}\sigma$) into a pore-throat is higher in cooler region than in warmer region. The pore-percolation favors the neighboring throat with minimum p_c, so air-liquid displacement prefers warmer direction, i.e., towards the region far away from the fracture-matrix interface. This evaporation-induced local cooling and sequential Marangoni effect can rationalize the "inside-out" drying pattern that we observe in experiments.

Nevertheless, for Marangoni effect to be important in the percolation sequence, its impact must be comparable or larger than other competing driving forces. In porous media flow-through drying, displacement pattern is also determined by 1) throat size distribution, and 2) pressure gradient resulted by viscous dissipation.

Marangoni effect's contribution to p_c can be quantified by $(\Delta\sigma_T/\sigma)\, p_c$; throat size difference's contribution to p_c can be quantified by $(\Delta w_t/w_t)\, p_c$ where Δw_t is throat size contrast (fabrication error in this work); viscous effect can be quantified by dissipation along the distance of a pore size, as $\frac{d_p+w_t}{l}\Delta p_{vis}$. Only when $(\Delta\sigma_T/\sigma)\, p_c$ is larger than both $(\Delta w_t/w_t)\, p_c$ and $\frac{d_p+w_t}{l}\Delta p_{vis}$ can Marangoni effect be dominant in shaping the fluid distribution pattern during flow-by drying.

4.2. Estimation of the effective cooling area A_{eff}

A simplified experimental model is shown schematically in Fig. 5. Based on the injected air flow rate the Pe number (Pe_f) in the fracture can be calculated as $Pe_f = \frac{v_{air} w_f}{D}$, respectively. D is the diffusion coefficient of pentane vapor ($D = 9.3 \times 10^{-6}\mathrm{m}^2/\mathrm{s}$ (Elliott and Watts, 1972)). For Case 1 and Case 2, Pe_f is much smaller than 1 so diffusion dominates. At the much higher air flow rate of Case 3, Pe_f is much larger than 1, indicating that convection dominates mass transfer in the fracture.

When the injection air flow rate is low, the characteristic diffusion length of the system is the fracture width (w_f), and the vapor takes the low temperature. Since diffusion is independent of pore structure and permeability, the diffusion of pentane vapor into the fracture at the evaporation surface is accompanied by the diffusion of a distant saturated pentane vapor towards the inlet of the injected air, and both have the same diffusion distance. The area characterized by diffusion at low injection flow rates is w_f^2, i.e., the effective cooling area for evaporation: $A_{eff} = 2w_f^2$.

As the injection air flow rate increases, convection begins to affect the evaporative heat and mass transfer process in porous media. At this

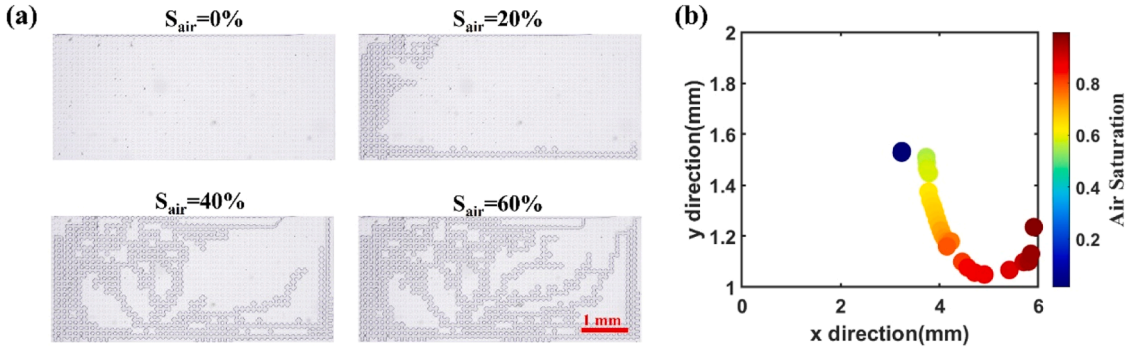

Fig. 4. (a) original experimental image of case 3 at different moments; (b) mass center trajectory during case 3. Dark regions indicate air-filled pores, whereas light/transparent regions indicate liquid-filled regions.

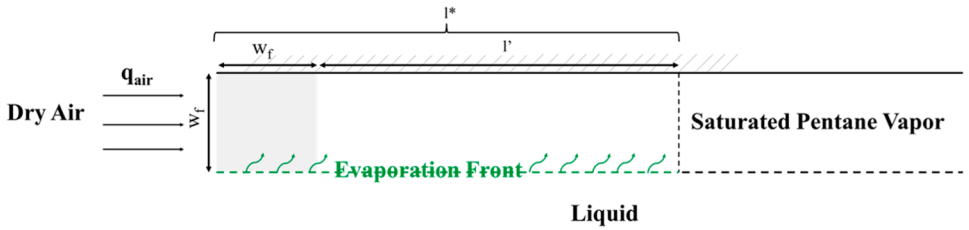

Fig. 5. Schematic diagram of transversal fracture area in experimental model.

time, the characteristic length of the system along the fracture(l^*) is the sum of the diffusion characteristic length and the convection characteristic length l'. l' is the distance that the fluid travels through the fracture at the average velocity during the fracture diffusion time, that is $l' = \tau_f \bar{v}$, where $\tau_f = \frac{w_f^2}{D}$ is the diffusion characteristic time in the fracture and $\bar{v} = \frac{1}{2}\left(1 + \frac{p_0}{p_0 - p_v}\right) v_{air}$ is the average velocity of the fluid in the transversal fracture. Therefore, when the injected air flow rate is large, the evaporation characteristic distance along the fracture direction is $l^* = w_f + l'$. The effective area of evaporative cooling is $A_{eff} = w_f l^* = 2w_f^2\left(1 + \overline{Pe_f}\right)$, where there is $\overline{Pe_f} = \frac{\bar{v} w_f}{D}$. We conduct more experiments with q_{air} varying from 3×10^{-6}ml/min to 6×10^{-1}ml/min, and all the observed fluid distribution patterns are shown in Figure. S1.

4.3. Estimation of temperature and surface tension contrast

The temperature contrast in the system can be estimated as $\Delta T_{est} = \frac{m_v \lambda}{K A_{eff}}$, where m_v is the mass flow rate of vapor, K is the effective heat transfer coefficient from the flow channel to the ambient environment, and A_{eff} is the effective cooling area. Accordingly, we can easily estimate the surface tension contrast induced by thermal effect as $\Delta\sigma_T = \frac{\partial \sigma}{\partial T}\Delta T_{est}$. We here neglect the surface tension contrast induced by pentane contaminant concentration gradient, $\Delta\sigma_C = \frac{\partial \sigma}{\partial C}\Delta C_{est}$, since we consider the high purity of pentane ensures highly uniform concentration gradient during the flowing and evaporating process.

It should be emphasized that the present glass micromodel system cannot be treated as an ideal adiabatic saturator since it continuously exchanges heat with both the surrounding glass and the ambient air. Heat can diffuse through the glass walls and partially replenish the evaporative cooling during air passage through the fracture. A characteristic comparison between air residence time in the fracture and thermal diffusion time through the glass is provided in Supplementary Text S3, which further shows the evident that current system cannot be treated adiabatically. Therefore, the Marangoni-relevant temperature contrast is not a constant bulk value determined only by the liquid–air pair, but a local and transient quantity that depends on evaporation rate, air flow rate, effective evaporation area, and heat supply from the surrounding glass. As a thermodynamic reference, we also estimate the adiabatic saturation temperatures of the pentane-air and isoheptane-air systems under the inlet conditions considered here (detailed calculation provided in Supplementary Text S3 and Table S1). However, the adiabatic saturation temperatures are only used as the thermodynamic reference, rather than as the actual Marangoni-driving temperature difference in the glass micromodel. The temperature contrast ΔT_{est} used in the present regime analysis represents an effective local temperature difference in the non-adiabatic system.

Assuming ideal air behavior and, as a first-order approximation, saturated outlet vapor, we get $m_v = M_g \frac{p_0 p_v}{p_0 - p_v}\frac{q_{air}}{RT}$. We also performed a simple mass-balance check of outlet vapor saturation (see Supplementary Text S4 and Table S2). The saturated-outlet assumption is most nearly satisfied for Marangoni case 2. Consider both the heat resistance across the glass chip and in the ambient environment, we get $K = \frac{1}{\frac{z_g}{2\kappa} + \frac{1}{k_{air}}}$ where k_{air} is natural convection heat transfer coefficient (5–20W/m^2/K in most practical scenario, and we take 10W/m^2/K for estimation). Based on estimation of evaporating front length along the fracture, we have $A_{eff} \sim 2w_f^2\left(1 + \overline{Pe_f}\right)$ where $\overline{Pe_f} = \frac{\bar{v} w_f}{D}$ is denoted by transversal fracture Peclect number and $\bar{v} = \frac{1}{2}\left(1 + \frac{p_0}{p_0 - p_v}\right) v_{air}$ is the average flow rate along fracture.

4.4. Hypothesis validation and phase diagram

Values of q_{air}, relative contribution of viscous effect ($\frac{d_p + w_t}{l}\Delta p_{vis}/p_c = \frac{d_p + w_t}{l} Ca_f$, denoted by Ca_p), ΔT_{est}, and relative contribution of Marangoni effect $\Delta\sigma_T/\sigma$, for three cases are listed in Table 1. Remind that $\Delta w_t/w_t$ is 2% in the glass microfluidic chip.

The calculation well matches experimental observations in three cases:

- In case 1, $\Delta\sigma_T/\sigma << \Delta w_t/w_t$, so Marangoni effect is negligible; $Ca_p << \Delta w_t/w_t$, so viscous effect is also negligible.
- In case 2, $\Delta\sigma_T/\sigma > \Delta w_t/w_t >> Ca_p$, so Marangoni effect is stronger than both pore-size contrast and viscous forcing. This makes Case 2 the clearest Marangoni-related case.
- In case 3, $\Delta w_t/w_t << \Delta\sigma_T/\sigma << Ca_p$, so the fluid distribution evolution is controlled mainly by viscous effect.

Accordingly, we define dimensionless number $Mp = (\Delta\sigma_T/\sigma)/(\Delta w_t/w_t)$ to characterize the relative significance of Marangoni effect to pore-size contrast, and $Mv = (\Delta\sigma_T/\sigma)/Ca_p$ to characterize the relative significance of Marangoni effect to viscous effect. Based on these two indicators, we construct the phase diagram in Fig. 6 as a mechanistic classification framework. In this framework, the dashed lines $Mv = 1$, $Mp = 1$ and $Mv = Mp$ represent the threshold conditions at which the Marangoni contribution becomes comparable to the competing effects. Specifically:

- Marangoni-related regime: $Mp > 1$, $Mv > 1$, where Marangoni effect is stronger than both pore-size contrast and viscous forcing. Case 2 falls most clearly in this regime.
- Isothermal regime: $Mp < 1$, $Mv/Mp > 1$, where both Marangoni and viscous effects are negligible. Case 1 corresponds to this regime.
- Viscous regime: $Mv < 1$ and $Mv/Mp < 1$, where viscous forcing dominates. Case 3 corresponds to this regime.

We use the liquid mass center offsets as an experimental diagnostic for regime classification. The normalized center offsets are defined as $O_x = \frac{x_{c,max} - x_{c,min}}{L_x}$ and $O_y = \frac{y_{c,max} - y_{c,min}}{L_y}$, where $L_x = 6mm$ and $L_y = 3mm$ are

Table 1
key variables and dimensionless numbers for case 1–4.

Case #	q_{air} (ml/min)	Ca_p (%)	ΔT_{est} (K)	$\Delta\sigma_T/\sigma$ (%)
Case 1	3×10^{-6}	0.001	0.016	0.01
Case 2	8×10^{-4}	0.30	3.77	2.68
Case 3	6×10^{-1}	218.25	34.93	24.77

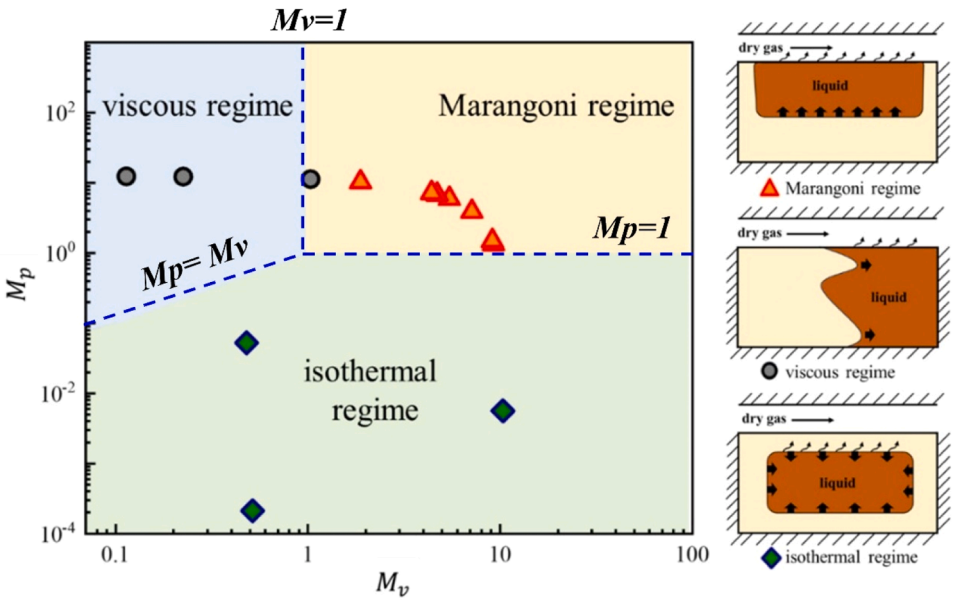

Fig. 6. Mechanistic phase diagram in the *Mv-Mp* space. Here, *Mp* characterizes the relative importance of Marangoni effect to pore-size contrast, and *Mv* characterizes the relative importance of Marangoni effect to viscous forcing. The dashed lines $Mv = 1$ and $Mp = 1$ mark the primary threshold conditions between competing controls, while the diagonal boundary $Mv/Mp = 1$ separates the viscous and isothermal regimes in the lower-left part of the diagram. The triangle indicates the Marangoni-related regime, the circle indicates the viscous regime, and the diamond indicates the isothermal regime. Symbols are assigned according to the liquid mass-center offsets. Regions close to the dashed lines should be interpreted as transition boundaries rather than sharp separations.

the length and width of the porous matrix. We identify cases belongs to the isothermal regime, when both O_x and O_y are smaller than 10%. Cases in Marangoni-related regime have O_x < 10% but O_y > 10%. In the viscous-dominated regime, both O_x and O_y exceed 10% and even larger. Therefore, M_v and M_p define the theoretical regime boundaries, whereas the symbols in Fig. 6 are assigned based on the experimental classification criteria derived from the liquid mass-center offsets. Slight discrepancies between the theoretical position and the experimental classification may occur.

Additional experiments with q_{air} varying from 3×10^{-6}ml/min to 6×10^{-1}ml/min show patterns broadly consistent with this framework, as summarized in Fig. 6.

4.5. Implications and limitations

1) **Decoupled drying fronts.** The non-classical 'inside-out' morphology implies that the evaporation front remains near the fracture while the displacement front penetrates deeper into the porous matrix. The clearest Marangoni-related manifestation of this behavior is observed in case 2, whereas the higher-flow case 3 involves stronger viscous effects. This decoupling maintains air–liquid contact near the fracture side and delays local dry-out relative to the classical front-recession pattern. However, this should not be interpreted as implying a universally higher global evaporation rate, because the overall evaporation rate may still be constrained by air throughput and vapor carrying capacity when the outlet air is close to saturation. In this sense, the main kinetic consequence of the inside-out morphology is to reshape the spatial distribution of evaporation and air invasion, rather than to guarantee faster overall drying.
2) **Implications for real subsurface fractured media.** In real three-dimensional fractured subsurface systems, heat dissipation away from the fracture may be less efficient than in the present thin glass micromodel, so that some local regions could behave closer to an adiabatic system. Under such conditions, evaporation-induced thermal gradients, and thus Marangoni effects, may become more pronounced. At the same time, the influences of pore-scale heterogeneity and three-dimensional fracture geometry are expected to be more complex and require more detailed investigation. From a thermodynamic and geochemical perspective, if non-volatile solute involves, the decoupled evaporation front and displacement front may reshape phase separation pattern, or retention within the porous media, as that during salt precipitation during flow-through drying in saline aquifer (Giorgis et al., 2007; Rufai and Crawshaw, 2017).
3) **Limitation of fluid system.** The relevance of the present pentane–air experiments to subsurface water–CO_2 systems or other gas-liquid combinations should be interpreted mainly at the mechanistic level rather than as a one-to-one quantitative analogy. The most relevant physical ingredients are the volatility (or saturation vapor pressure) of the liquid, the latent heat of vaporization, the sensitivity of interfacial tension to temperature, the heat supply from the surrounding solid/fluid phases, and the capillary resistance of the porous medium. Together, these factors determine whether evaporation can generate sufficiently strong local cooling and interfacial thermal gradients to modify the drying morphology. If evaporation-induced surface-tension gradients are too weak under a given subsurface condition, the specific Marangoni-related behavior highlighted here may be weak or absent.
4) **Limitation of geometry and scale.** The experiments are conducted on a 2D microfluidic glass model, which might not fully represent the complexities of natural subsurface media and engineering porous media (Xu et al., 2008). Even though the pore heterogeneities in real subsurface could hinder global thermal equilibrium which contributes the Marangoni flow, some local places where rocks have higher thermal conductivity, e.g., carbonate rock is about 4–6W/K/m that much higher than glass, which may suppress local Marangoni flows. In addition, the experiments are primarily conducted in ambient conditions with reachable boundary and complete evaporation, so its applicability to wider range remains to be tested (Schwartze and Bröcker, 2000; Costa and da Silva, 2003). The scale of experiment is also not large enough to capture long-term effects, such as the period that molecular diffusion controls the kinetics. Further effort is required to clarify its up-scaled behavior, and incorporate it into numerical modeling and theoretical evaluation methods.

5) **Possible alternative explanations.** We further note that other factors may also influence the detailed drying morphology. First, the exact outlet saturation state and vapor-removal pathway remain uncertain, very small leakage or unquantified vapor exchange cannot be fully excluded without direct outlet measurements. However, gas leakage is not observed during the experiments, and the gas phase remains confined within the designed micromodel domain. Second, wettability effects are not directly measured. Because the micromodel surface is glass throughout the pore network, we expect large spatial wettability variations to be limited. Third, pore-scale heterogeneity is expected to be relatively small because the internal post array is nominally homogeneous and the measured internal throat-size variation is smaller than the widened peripheral boundary regions. Overall, these factors may influence local invasion details, but the Marangoni-related interpretation is supported by the combined evidence from volatility contrast, flow-rate dependence, delayed fracture-side dry-out, matrix-interior invasion, observed evaporative cooling in the supplementary thermal experiment, and the known temperature dependence of pentane–air interfacial tension.

5. Conclusion

We demonstrated the significant role of evaporation-induced Marangoni effect during flow-by drying in porous media based on microfluidic experiments and theoretical analysis. It may bring major consequences in CO_2 sequestration, hydrogen storage, natural gas recovery, fuel cell water management and other potential geophysical, geochemical and engineering applications. It also provides new insights into the coupling of fluid flow, phase change and thermal effects in disordered media.

We discovery a surprising “inside-out” drying pattern, for gas flow rate ranging over several orders of magnitude. We hypothesize that it is attributed to Marangoni effect, that temperature contrast generated by evaporation modifies capillary entrance pressure field, thus induces gas percolation towards warmer and deeper porous matrix. Theoretical analysis supports this hypothesis, and reveals that Marangoni effect is competing with viscous effect and throat size distribution in determination of pore-percolation sequence. We propose a theoretical phase diagram to identify different fluid evolution patterns (isothermal regime, Marangoni regime and viscous regime) during flow-by drying in porous media adjacent to a gas-flowing fracture in the system, which is further validated by more experiments.

The present results provide mechanistic insight into how strong evaporation-induced local thermal effects can reshape pore-scale drying morphology. The “inside-out” pattern during flow-by drying in porous media adjacent to a gas-flowing fracture may delays local dry-out and improves gas storage stability than that predicted by classic isothermal models. More efforts are thus required to upscale it to macroscopic scale, and incorporate its effects into field-scale models.

Open research

Experimental data and phase diagram calculations supporting the results of this study are publicly available at Peking University Open Research Data Platform via (https://doi.org/10.18170/DVN/SGHOAZ), (Fei, 2024).

CRediT authorship contribution statement

Yandong Zhang: Writing – review & editing, Writing – original draft, Methodology, Investigation, Formal analysis, Data curation, Conceptualization. **Fei Yu:** Writing – review & editing, Visualization, Software, Methodology, Investigation, Formal analysis, Data curation. **Shuai Zheng:** Software, Methodology, Investigation, Formal analysis, Data curation. **Bowen Ling:** Writing – review & editing, Validation, Resources, Conceptualization. **Dongxiao Zhang:** Writing – review & editing, Supervision, Conceptualization. **Ke Xu:** Writing – review & editing, Supervision, Resources, Project administration, Funding acquisition, Conceptualization.

Declaration of competing interest

The authors declare that they have no known competing financial interests or personal relationships that could have appeared to influence the work reported in this paper.

Acknowledgments

We gratefully acknowledge the financial support and funding provided by National Natural Science Foundation of China under Grant No U23B6004, by National Key Research and Development Project of China under Grant No 2023YFA1011700.

Supplementary materials

Supplementary material associated with this article can be found, in the online version, at doi:10.1016/j.advwatres.2026.105367.

Data availability

I have shared the link to my data in main text "OPEN RESEARCH" section

References

Ahmad, F., Rahimi, A., Tsotsas, E., Prat, M., Kharaghani, A., 2021. Int. J. Heat Mass Transf. 165, 120722.
Allerton, J., 1948. University of Michigan.
Andersen, O., Nilsen, H.M., 2018. Int. J. Greenh. Gas Control 72, 49–64.
Attari Moghaddam, A., Kharaghani, A., Tsotsas, E., Prat, M., 2017. Phys. fluids 29.
Carmo, M., Fritz, D.L., Mergel, J., Stolten, D., 2013. Int. J. Hydrog. Energy 38, 4901–4934.
Chauvet, F., Duru, P., Geoffroy, S., Prat, M., 2009. Phys. Rev. Lett. 103, 124502.
Chraibi, H., Prat, M., Chapuis, O., 2009. Phy. Rev. E 79, 026313.
Costa, V., da Silva, F.N., 2003. Int. J. Heat Mass Transf. 46, 3717–3726.
D'Aubeterre, A., Silva, R.Da, Aguilera, M., 2005. Int. Commun. Heat Mass Transf. 32, 677–684.
Ding, Y., Geistlinger, H., 2021. Water Resour. Res. 57, e2021WR029861.
Edery, Y., Berg, S., Weitz, D., 2018. Phys. Rev. Lett. 120, 028005.
Elliott, R.W., Watts, H., 1972. Can. J. Chem. 50, 31–34.
Y. Fei, (Peking University Open Research Data Platform, 2024).
Geistlinger, H., Ding, Y., Apelt, B., Schlüter, S., Küchler, M., Reuter, D., Vorhauer, N., Vogel, H.J., 2019. Water Resour. Res. 55, 6653–6672.
Giorgis, T., Carpita, M., Battistelli, A., 2007. Energy Convers. Manag. 48, 1816–1826.
Gourbil, A., Fichot, F., Prat, M., Quintard, M., Duru, P., 2019. Exp. Therm. Fluid Sci. 107, 140–145.
Grigoryev, B.A., Nemzer, B.V., Kurumov, D.S., Sengers, J.V., 1992. Int. J. Thermophys. 13, 453–464.
Hilfer, R., Øren, P., 1996. Transp. Porous Media 22, 53–72.
Huinink, H., Pel, L., Michels, M., Prat, M., 2002. Eur. Phys. J. E 9, 487–498.
Jagannathan, Mahadevan, Mukul, M., Sharma, Yannis, C., Yortsos, 2006. Aiche J.
Jiao, K., et al., 2021. Nature 595, 361–369.
Kamath, J., Laroche, C., 2003. SPE J. 8, 71–80.
Krevor, S., et al., 2023. Nat. Rev. Earth Environ. 4, 102–118.
Lehmann, P., Assouline, S., Or, D., 2008. Phys. Rev. E 77, 056309.
Mahadevan, J., Sharma, M.M., 2003. SPE Annual Technical Conference and Exhibition? SPE. SPE.
Mahadevan, J., Sharma, M.M., Yortsos, Y.C., 2006. AIChE J. 52, 2367–2380.
Milly, P.C.D., 1984. Water Resour. Res. 20, 1075–1085.
Ott, H., Andrew, M., Snippe, J., Blunt, M.J., 2014. Geophys. Res. Lett. 41, 8369–8376.
Ott, H., Roels, S., De Kloe, K., 2015. Int. J. Greenh. Gas Control 43, 247–255.
Park, J., Oh, H., Ha, T., Lee, Y.I., Min, K., 2015. Appl. Energy 155, 866–880.
Peysson, Y., André, L., Azaroual, M., 2014. Int. J. Greenh. Gas Control 22, 291–300.
Pillai, K., Prat, M., Marcoux, M., 2009. Int. J. Heat Mass Transf. 52, 1643–1656.
Plourde, F., Prat, M., 2003. Int. J. Heat Mass Transf. 46, 1293–1307.
Prat, M., 2002. Chem. Eng. J. 86, 153–164.
Prat, M., 2007. Int. J. Heat Mass Transf. 50, 1455–1468.
Prat, M., 2011. Chem. Eng. Technol. 34, 1029–1038.
Rufai, A., Crawshaw, J., 2017. Phys. Fluids 29.
Scherer, G.W., 1990. J. Am. Ceram. Soc. 73, 3–14.
Schwartze, J., Bröcker, S., 2000. Int. J. Heat Mass Transf. 43, 1791–1800.
Shokri, N., Lehmann, P., Or, D., 2009. Water Resour. Res. 45.
Sim, S., Turtata, A., Singhal, A., Hawkins, B., 2009. J. Can. Pet. Technol. 48, 49–55.

Surasani, V., Metzger, T., Tsotsas, E., 2008a. Int. J. Heat Mass Transf. 51, 2506–2518.
Surasani, V., Metzger, T., Tsotsas, E., 2008b. Chem. Eng. Sci. 63, 5218–5228.
Surasani, V., Metzger, T., Tsotsas, E., 2009. Transp. Porous Media 80, 431–439.
Surasani, V., Metzger, T., Tsotsas, E., 2010. Dry. Technol. 28, 615–623.
Vilarrasa, V., Rutqvist, J., 2017. Earth-Sci. Rev. 165, 245–256.
Vorhauer, N., Wang, Y., Kharaghani, A., Tsotsas, E., Prat, M., 2015. Transp. Porous Media 110, 197–223.
Vorhauer, N., Tsotsas, E., Prat, M., 2018. Phys. Rev. Fluids 3, 114201.
Xu, L., Davies, S., Schofield, A.B., Weitz, D.A., 2008. Phys. Rev. Lett. 101, 094502.
Yiotis, A., et al., 2005. Pore-network modeling of isothermal drying in porous media. Transport in Porous Media 58 (1), 63–86.
Zivar, D., Kumar, S., Foroozesh, J., 2021. Int. J. Hydrog. Energy 46, 23436–23462.